

***Euclid*: Early Release Observations – A glance at free-floating new-born planets in the σ Orionis cluster[★]**

E. L. Martín^{1,2}, M. Žerjal^{1,2}, H. Bouy^{3,4}, D. Martín-Gonzalez⁵, S. Muñoz Torres^{1,2}, D. Barrado⁶, J. Olivares⁷, A. Pérez-Garrido⁸, P. Mas-Buitrago⁶, P. Cruz⁶, E. Solano⁶, M. R. Zapatero Osorio⁶, N. Lodieu^{1,2}, V. J. S. Béjar^{1,2}, J.-Y. Zhang^{1,2}, C. del Burgo^{1,2}, N. Huélamo⁶, R. Laureijs⁹, A. Mora¹⁰, T. Saifollahi^{11,12}, J.-C. Cuillandre¹³, M. Schirmer¹⁴, R. Tata¹⁵, S. Points¹⁶, N. Phan-Bao^{17,18}, B. Goldman^{19,11}, S. L. Casewell²⁰, C. Reylé²¹, R. L. Smart^{22,23}, N. Aghanim²⁴, B. Altieri²⁵, S. Andreon²⁶, N. Auricchio²⁷, M. Baldi^{28,27,29}, A. Balestra³⁰, S. Bardelli²⁷, A. Basset³¹, R. Bender^{32,33}, D. Bonino²², E. Branchini^{34,35,26}, M. Brescia^{36,37,38}, J. Brinchmann³⁹, S. Camera^{40,41,22}, V. Capobianco²², C. Carbone⁴², J. Carretero^{43,44}, S. Casas⁴⁵, M. Castellano⁴⁶, S. Cavuoti^{37,38}, A. Cimatti⁴⁷, G. Congedo⁴⁸, C. J. Conselice⁴⁹, L. Conversi^{50,25}, Y. Copin⁵¹, L. Corcione²², F. Courbin⁵², H. M. Courtois⁵³, M. Cropper⁵⁴, A. Da Silva^{55,56}, H. Degaudenzi⁵⁷, A. M. Di Giorgio⁵⁸, J. Dinis^{55,56}, F. Dubath⁵⁷, X. Dupac²⁵, S. Dusini⁵⁹, A. Ealet⁵¹, M. Farina⁵⁸, S. Farrens¹³, S. Ferriol⁵¹, P. Fosalba^{60,61}, M. Frailis⁶², E. Franceschi²⁷, M. Fumana⁴², S. Galeotta⁶², B. Garilli⁴², W. Gillard⁶³, B. Gillis⁴⁸, C. Giocoli^{27,64}, P. Gómez-Alvarez^{65,25}, A. Grazian³⁰, F. Grupp^{32,33}, L. Guzzo^{66,26}, S. V. H. Haugan⁶⁷, J. Hoar²⁵, H. Hoekstra⁶⁸, W. Holmes⁶⁹, I. Hook⁷⁰, F. Hormuth⁷¹, A. Hornstrup^{72,73}, D. Hu⁵⁴, P. Hudelot⁷⁴, K. Jahnke¹⁴, M. Jhabvala⁷⁵, E. Keihänen⁷⁶, S. Kermiche⁶³, A. Kiessling⁶⁹, M. Kilbinger⁷⁷, T. Kitching⁵⁴, R. Kohley²⁵, B. Kubik⁵¹, M. Kümmel³³, M. Kunz⁷⁸, H. Kurki-Suonio^{79,80}, D. Le Mignant⁸¹, S. Ligori²², P. B. Lilje⁶⁷, V. Lindholm^{79,80}, I. Lloro⁸², D. Maino^{66,42,83}, E. Maiorano²⁷, O. Mansutti⁶², O. Marggraf⁸⁴, N. Martinet⁸¹, F. Marulli^{85,27,29}, R. Massey⁸⁶, E. Medinaceli²⁷, S. Mei⁸⁷, M. Melchior⁸⁸, Y. Mellier^{89,74}, M. Meneghetti^{27,29}, G. Meylan⁵², J. J. Mohr^{33,32}, M. Moresco^{85,27}, L. Moscardini^{85,27,29}, S.-M. Niemi⁹, C. Padilla⁹⁰, S. Paltani⁵⁷, F. Pasian⁶², K. Pedersen⁹¹, W. J. Percival^{92,93,94}, V. Pettorino⁹, S. Pires¹³, G. Polenta⁹⁵, M. Poncet³¹, L. A. Popa⁹⁶, L. Pozzetti²⁷, G. D. Racca⁹, F. Raison³², R. Rebolo^{1,2}, A. Renzi^{97,59}, J. Rhodes⁶⁹, G. Riccio³⁷, Hans-Walter Rix¹⁴, E. Romelli⁶², M. Roncarelli²⁷, E. Rossetti²⁸, R. Saglia^{33,32}, D. Sapone⁹⁸, B. Sartoris^{33,62}, M. Sauvage¹³, R. Scaramella^{46,99}, P. Schneider⁸⁴, A. Secroun⁶³, G. Seidel¹⁴, M. Seiffert⁶⁹, S. Serrano^{60,100,101}, C. Sirignano^{97,59}, G. Sirri²⁹, L. Stanco⁵⁹, P. Tallada-Crespí^{43,44}, A. N. Taylor⁴⁸, H. I. Teplitz¹⁰², I. Tereno^{55,103}, R. Toledo-Moreo¹⁰⁴, A. Tsyganov¹⁰⁵, I. Tutusaus¹⁰⁶, L. Valenziano^{27,107}, T. Vassallo^{33,62}, G. Verdoes Kleijn¹², Y. Wang¹⁰², J. Weller^{33,32}, O. R. Williams¹⁰⁵, E. Zucca²⁷, C. Baccigalupi^{108,62,109,110}, G. Willis⁵⁴, P. Simon⁸⁴, J. Martín-Fleitas¹⁰, and D. Scott¹¹¹

(Affiliations can be found after the references)

May 24, 2024

ABSTRACT

We provide an early assessment of the imaging capabilities of the *Euclid* space mission to probe deeply into nearby star-forming regions and associated very young open clusters, and in particular to check to what extent it can shed light on the new-born free-floating planet population. This paper focuses on a low-reddening region observed in just one *Euclid* pointing where the dust and gas has been cleared out by the hot σ Orionis star. One late-M and six known spectroscopically confirmed L-type substellar members in the σ Orionis cluster are used as benchmarks to provide a high-purity procedure to select new candidate members with *Euclid*. The exquisite angular resolution and depth delivered by the *Euclid* instruments allow us to focus on bona-fide point sources. A cleaned sample of σ Orionis cluster substellar members has been produced and the initial mass function (IMF) has been estimated by combining *Euclid* and *Gaia* data. Our σ Orionis substellar IMF is consistent with a power-law distribution with no significant steepening at the planetary-mass end. No evidence of a low-mass cutoff is found down to about 4 Jupiter masses at the young age (3 Myr) of the σ Orionis open cluster.

Key words. Surveys – Astronomical instrumentation, methods and techniques – open clusters and associations: σ Orionis – Techniques: photometric – Stars: imaging

1. Introduction

The nearest star-forming regions provide us with a natural laboratory to investigate in detail the complex processes that trans-

* This paper is published on behalf of the Euclid Consortium.

** e-mail: ege@iac.es

form molecular clouds into stellar and substellar-mass objects. In particular, one of the long-standing questions is whether or not there is a low-mass cutoff in the initial mass function (IMF). The original IMF was defined by [Salpeter \(1955\)](#) as a single power-law function over the mass range from 10 down to 0.4 Solar masses (M_{\odot}). While the early computations of spherical collapse including dust-grain opacities found a minimum mass of $0.1 M_{\odot}$ owing to opacity-limited fragmentation, i.e., above the substellar-mass limit ([Silk 1977](#)), recent calculations predict that the minimum fragment could reach down to $10^{-3} M_{\odot}$ ([Mondal & Chattopadhyay 2019](#)), i.e. well below the deuterium-burning mass limit. The thermonuclear fusion of deuterium, ${}^2\text{H}(p,\gamma){}^3\text{He}$, takes place at 10^6 K and can be important in the early stages of evolution of objects with masses above 13 times the mass of Jupiter ($1 M_{\text{J}} = 0.000955 M_{\odot}$); see [Bodenheimer \(1966\)](#), [Stahler \(1988\)](#), and [Chabrier et al. \(2000\)](#).

Deep observations of stellar nurseries, very young open clusters, and young stellar associations have been made to search for the predicted low-mass cutoff of the IMF, and they have reported that the IMF extends smoothly into the realm of planetary masses, reaching down to the deuterium limit and overlapping with the masses of exoplanets. Various names have been used to refer to these unexpected substellar-mass objects, such as, for example, brown dwarfs (BDs) of planetary mass, sub-brown dwarfs, cluster planets, nomadic worlds, free-floating planets (FFPs), rogue planets, and planetary-mass objects (PMOs). Collectively, substellar-mass objects are ultracool dwarfs (UCDs) with very cool effective temperatures, late spectral types, small sizes and faint luminosities that make them appear to be a tiny minority among the myriad of stars and galaxies in deep astronomical surveys, even though their numbers can be significant.

Free-floating planets appear to be ubiquitous and numerous, since they have been identified by direct imaging and spectroscopy in many different stellar cradles. Some examples of such targets are: the Chamaeleon I star-forming region ([Oasa et al. 1999](#); [Luhman et al. 2004](#)); the IC 348 and NGC 1333 clusters in Perseus ([Esplin & Luhman 2017](#); [Scholz et al. 2023](#)); the Ophiucus star-forming region ([Chiang & Chen 2015](#); [Bouy et al. 2022](#)); the Orion Nebula cluster ([Lucas & Roche 2000](#); [Lucas et al. 2001, 2006](#)); the Lynds 1630 molecular clouds ([Spezzi et al. 2015](#)), the σ Orionis ([Zapatero Osorio et al. 2000](#); [Lodieu et al. 2009](#)) and Collinder 69 ([Bayo et al. 2011](#)) young clusters in the Orion giant star-formation complex; the Upper Sco OB association ([Lodieu et al. 2018, 2021](#); [Miret-Roig et al. 2022](#)); and the Taurus dark clouds ([Esplin & Luhman 2019](#)). PMOs have also been found as wide companions to stars and BDs ([Chauvin et al. 2005](#); [Gauza et al. 2015](#)), as members of young moving associations ([Zhang et al. 2021](#)), and as microlensing events towards the Galactic bulge ([Mróz et al. 2018](#); [Koshimoto et al. 2023](#); [Sumi et al. 2023](#)).

The existence of FFPs challenges models of star and planet formation. A variety of physical mechanisms have been proposed to explain the formation of substellar objects with masses well below the Jeans limit, the leading one being turbulent fragmentation ([Padoan & Nordlund 2004](#); [Hennebelle & Chabrier 2008](#)), but others, including gravitational collapse in filaments, ejection from proto-planetary discs, and photo-erosion ([Miret-Roig 2023](#)) have not been discarded as potential players.

The cosmologically-driven requirements of the *Euclid* mission ([Laureijs et al. 2011](#)) and the performance of its VIS ([Euclid Collaboration: Cropper et al. 2024](#)) and NISP ([Euclid Collaboration: Jahnke et al. 2024](#)) instruments are expected to enable a major leap in sensitivity gain and area coverage that will foster the advance of many areas of legacy science in astrophysics ([Eu-](#)

[clid Collaboration: Mellier et al. 2024](#)), including the detection of around a million UCDs over a large portion of the Milky Way ([Solano et al. 2021](#); [Martin et al. 2023](#)), with spectroscopic reconnaissance spectra for thousands of them ([Martín et al. 2021](#); [Jun-Yan Zhang et al. 2024](#)). The *Euclid* reference observing sequence (ROS) is the main observation mode that is used for the wide and deep surveys. It is required to reach limiting AB magnitudes of 26.2 in the optical I_E band and of 24.5 in the near-infrared NISP bands over a wide area ([Euclid Collaboration: Scaramella et al. 2022](#)).

The *Euclid* Early Release Observations (ERO) programme has been designed to be a showcase of the mission's potential for legacy science across a wide range of sky regions. It demonstrates that *Euclid* brings a unique combination of unprecedented sensitivity, wide-area coverage, and high spatial resolution to the investigation of diverse science topics. The first ERO papers include studies of very high-redshift objects ([Weaver et al. 2024](#)), clusters of galaxies ([Kluge et al. 2024](#); [Marleau et al. 2024](#); [Saifollahi et al. 2024](#)), nearby galaxies ([Hunt et al. 2024](#)), and galactic globular clusters ([Massari et al. 2024](#)).

This ERO paper investigates the power of *Euclid* to probe deep into very young regions over a wide area, reaching detection limits capable of revealing the FFP population and eventually search for the predicted low-mass cutoff of the IMF. The paper is structured as follows. In Sect. 2, the general *Euclid* ERO project number 2 (ERO02, P.I. Martín) is presented. Five *Euclid* pointings were obtained and this work focuses in about half of the area covered by one of them. In Sect. 3, the particular region that is the focus of this work is described and in Sect. 4 previously known substellar-mass objects in the σ Orionis cluster are discussed and the cuts used to select new FFP candidates are described. Section 5 deals with the revised initial mass function (IMF) of the σ Orionis cluster in the area covered by the *Euclid* observations and comparison with the field IMF low-mass tail. Finally, Sect. 6 summarises our results and provides future prospects.

2. The *Euclid* Early Release Observations project of nearby star-forming regions

This *Euclid* ERO programme has targeted nearby (distance ≤ 400 pc) star-forming regions and very young open clusters (age < 10 Myr) to explore their faint ultra-cool populations, search for FFPs, and determine whether or not there is an IMF low-mass cutoff. The total project consists of five *Euclid* pointings. The targets were the following: the NGC 1333 cluster in Perseus (incomplete dataset); the Barnard 30, Barnard 33 (Horsehead nebula, that also includes the NGC 2023 embedded cluster and part of the σ Orionis open cluster), and Messier 78 dark clouds in the Orion star-formation complex, and a field containing several dark clouds in the Taurus region. In this paper we focus on one of these targets, called the Horsehead field, and in particular we focus on about half of the area, hereafter nicknamed the ERO-SOri field. The other regions covered by the *Euclid* ERO pointings will be the subject of future studies.

The *Euclid* observation of the ERO-SOri field took place on 2 October 2023. A full ROS with good guiding was obtained. The centre coordinates of each of the four *Euclid* exposures that make up the ROS were the following: $85^{\circ}150915, -2^{\circ}613342$; $85^{\circ}167068, -2^{\circ}582078$; $85^{\circ}166265, -2^{\circ}551255$; and $85^{\circ}182417, -2^{\circ}519991$. The full FoV of the ERO pointing presented here is displayed in Fig. 1 and covers an area of 0.58 square degrees. The FoV was chosen to avoid the blinding star σ Orionis and to

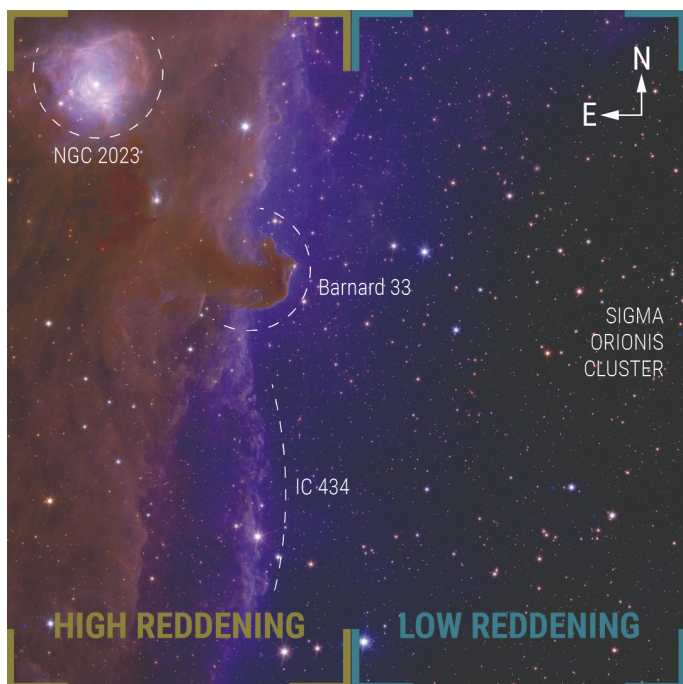


Fig. 1. Multi-colour mosaic of the *Euclid* pointing studied in this work. The area covered is 0.58 square degrees. The dark neck of the Horse-Head (Barnard 33) is pointing towards the bright σ Orionis star, located just outside the field of view (FoV). The bright nebular emission crossing the image is the IC 434 H II region, and the bright concentration at the upper left corner is NGC 2023. This paper focuses on the low reddening part of the FoV that has been cleared out by the hot σ Orionis star.

include the Barnard 33 molecular cloud (Horsehead Nebula), the NGC 2023 cluster and reflection nebula, and the IC 434 H II region. The full *Euclid* ROS consisted of four dithered exposures in VIS and NISP using the nominal exposure times described in [Euclid Collaboration: Cropper et al. \(2024\)](#) and [Euclid Collaboration: Jahnke et al. \(2024\)](#), respectively. The dithering pattern is designed so that the gaps between the detectors can be covered when making a stack of the four images. However, due to a failure in the implementation of the dithering during the science-verification phase, the pattern was not optimised and there are some gaps in the mosaic of this ERO footprint. Furthermore, during data processing it was realised that about 5% of the FoV was covered by only one image and cosmic rays could not be removed efficiently. After data reduction and image stacking, following the procedures described in [Cuillandre et al. \(2024\)](#), the data have been validated and considered ready for science exploitation. In this work, the catalogues and images of the ERO public data release are used ([Euclid Early Release Observations 2024](#)). They do not include any spectroscopic data.

3. The region covered in the ERO observation

The ERO pointing shown in Fig. 1 contains the complex region created by the interaction between the hot σ Orionis star and the Orion B giant molecular cloud (Lynds 1630). Extreme ultraviolet radiation from the O-type star σ Orionis creates a bright ionisation front that is known as the IC 434 H II region. A complicated pattern of bright and dark regions is clearly seen in fine detail in the *Euclid* mosaic (Fig. 1). The Horsehead Nebula (Barnard 33) is projected in the foreground of the H II region at a distance of around 360 pc and it points towards the ionising σ Orionis

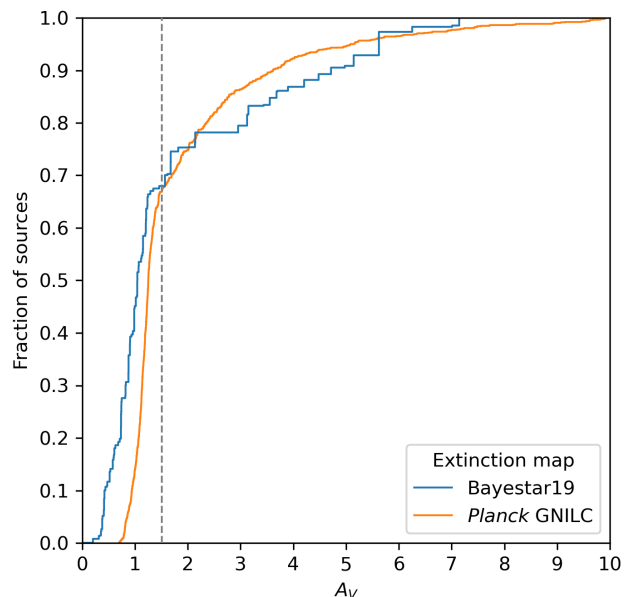


Fig. 2. Cumulative distribution of interstellar reddening in the *Euclid* ERO region shown in Fig. 1. Two different methods of estimating the reddening are compared. Note that about 70% of the FoV has a modest reddening of less than 1.7 mag in the visual. This reddening is used in the reddening vectors shown in the colour-magnitude and u-colour diagrams. This work focuses on the low-reddening region of the FoV.

star that is in the background ([Bally et al. 2018](#)). Another source of ionisation in the ERO-SOri FoV is the B-type star HD 37903 that illuminates a reflection nebula and is associated with the embedded open cluster NGC 2023 that contains very young low-mass stars ([Depoy et al. 1990](#); [Mookerjee et al. 2009](#); [Kounkel et al. 2017](#)). As a consequence of the complex past and ongoing star-formation processes, there are patches with significant interstellar reddening. The A_V extinction values for all the sources identified in this ERO pointing have been calculated with two extinction maps from the literature: the generalised needlet internal linear combination map from [Planck Collaboration \(2016\)](#), which is a 2D extinction map, and Bayestar19 ([Green 2018](#); [Green et al. 2019](#)), which is a 3D extinction map for which we assumed a mean distance of 400 pc to the Orion star-forming region. Both extinction maps were queried with the `dustmap`¹ package. The cumulative distribution function of the A_V extinction of our sources is shown in Fig. 2, where the curves depict the distributions of the two extinction maps from the literature and the vertical dashed line shows the maximum extinction value that our selection criteria can cover. As can be observed, both extinction maps agree quite well and show that about 70% of the sources in the FoV have A_V values between 0 and 1.7 mag. In the future we plan to use more specific methods that take into account the extinction of the individual sources (e.g., [Olivares et al. 2021](#)).

4. The *Euclid* view of the σ Orionis substellar members

The *Euclid* footprint of the ERO pointing includes a portion of the well-known σ Orionis cluster that has been a favourite hunt-

¹ <https://dustmaps.readthedocs.io/en/latest/index.html>

ing ground for very young substellar objects and FFPs for over two decades (Zapatero Osorio et al. 2000; Damian et al. 2023). A review of the σ Orionis cluster properties was provided by Walter et al. (2008). A recent assessment of cluster membership using the *Gaia* third data release (DR3, Gaia Collaboration et al. 2023) has been carried out in a study of the young populations in the region (Žerjal et al. 2024). The ages of most σ Orionis cluster members are in the range 1–5 Myr (Zapatero Osorio et al. 2002; Žerjal et al. 2024). In this work an age of (3 ± 2) Myr and a distance of 402.74 ± 9 pc are adopted for the σ Orionis cluster. The deepest survey carried out to date in the search for FFPs belonging to σ Orionis has been reported by Peña Ramírez et al. (2012) using ground-based telescopes.

4.1. Definition of benchmarks for *Euclid* based on confirmed σ Orionis substellar objects

We selected seven confirmed substellar-mass members of the σ Orionis cluster with ground-based low-resolution optical and near-infrared spectroscopic classification. Their names and coordinates are listed in Table 1, together with the spectral types from the literature (Zapatero Osorio et al. 2000; Barrado y Navascués et al. 2001; Martín et al. 2001; Zapatero Osorio et al. 2017). The parameters of these seven benchmarks in the *Euclid* ERO catalogue are listed in Table 2.

Table 1. Benchmark σ Orionis cluster members observed with *Euclid*.

Nickname	RA	Dec	Spectral type
	[hh mm ss.ss]	[deg mm ss.s]	
S Ori 28	05 39 23.19	−02 46 55.8	M5.5
S Ori 52	05 40 09.20	−02 26 32.0	L0.5
S Ori 60	05 39 37.50	−02 30 42.0	L2.0
S Ori 62	05 39 42.05	−02 30 31.6	L4.0
S Ori 054017	05 40 17.34	−02 36 22.6	L3.5
S Ori 054000	05 40 00.04	−02 40 33.1	L2.0
S Ori 054037	05 40 37.82	−02 40 01.1	L4.5

The values of the SPREAD_MODEL parameter for the benchmarks in all the *Euclid* passbands have very small deviations from zero, as expected for bona-fide point sources. This parameter was developed as a star/galaxy classifier by the data management pipeline of the Dark Energy Survey (Mohr et al. 2012), and has been shown to be a good discriminant for point sources in nearby young clusters and stellar associations (Bouy et al. 2013). The parameter is adopted in this work as one of the main selection criteria to separate point sources from galaxies.

We note that two benchmarks, namely S Ori 52 and 60, have FWHM_IMAGE_I values in the ERO catalogue that are slightly larger than the other four benchmarks, suggesting that they might be binaries that have angular separations close to the limit of spatial resolution of the VIS data. Moreover, a resolved faint visual companion was spotted close to S Ori 52 at position J054009.36−022631.93 in the VIS image (see Fig. 3). S Ori 52 has an optical spectral type of L0.5 and a mass around $15 M_J$ (Béjar et al. 2001). The candidate wide companion to S Ori 52 is 3.2 mag fainter in the I_e passband than the primary, the angular separation is $0''.962$ (387 au at 402 pc) and the position angle is $43^\circ.3$. The pair is not fully resolved in the NISP images because they have lower spatial resolution than the VIS image. Using PSF photometry, the difference in magnitude in the J_e passband is 3.96. This difference is larger than in I_e , indicating that the companion has slightly bluer $I_e - J_e$ colour than the primary and

casting some doubt on the physical association of these two objects. The possibility that *Euclid* may have found two substellar binaries, close to the angular resolution of the VIS images, in a sample of only seven benchmarks in the σ Orionis cluster, is interesting and deserves further scrutiny. A *Hubble* Space Telescope (HST) imaging survey of wide binaries (projected semi-major axes between 100 and 1000 au) among pre-main-sequence (PMS) stars in the Orion star-forming complex found a binary frequency of $12.5^{+1.2}_{-0.8}\%$ (Kounkel et al. 2016), and recent work with the *James Webb* Space Telescope suggests that substellar-mass binaries in the Trapezium cluster could be common (McCaughrean & Pearson 2023). On the other hand, no resolved binaries with separations > 20 au were found in an imaging survey of 33 BDs in two young open clusters (ages in the range from 70 to 120 Myr) carried out with the HST (Martín et al. 2003).

4.2. Contamination estimates and definition of selection cuts for the *Euclid* data

To assess the likelihood of contamination of substellar object candidates by background extragalactic objects and by foreground ultracool dwarfs, all the objects not saturated in the *Euclid* images and listed by Peña Ramírez et al. (2012) in the ERO-S Ori FoV were visually inspected in the VIS and NISP images and were cross-correlated with the ESO VISTA Hemisphere Survey (VHS) catalogue (McMahon et al. 2021) to check for proper motions. The total proper motion of true cluster members is expected to be ≤ 20 mas per year, and thus should not be measurable when comparing VHS and NISP data. A summary of the results of this contamination assessment is provided in Table 3. Sources that are spatially resolved as extended objects in any of the *Euclid* passbands are considered as non-members. They have values of the FWHM and SPREAD_MODEL parameters larger than those of the benchmarks. Sources that are detected to move by ≥ 100 mas from the VHS epoch to the *Euclid* epoch (baseline 14 years) are classified as non-members and are labelled as high proper motion. For the benchmarks, we checked that their coordinates match within 100 mas with those from the VHS catalogue. As expected, the most frequent contamination comes from extended objects that are probably background galaxies (9/38 = 24%), particularly at the faint end of the sample. The ratio of extragalactic sources to ultracool dwarfs is expected to get larger with increasing depth. It has recently been reported from JWST/NIRSpec spectroscopic follow-up of photometrically selected JWST/NIRCam compact sources that the ratio between extragalactic objects and ultracool dwarfs is 11/3 at depths fainter than those reached by the *Euclid* images (Langeroodi & Hjorth 2023).

The contamination by background extragalactic sources, the inhomogeneous interstellar extinction in star-forming regions, the possible presence of colour-excesses owing to discs and accretion activity, and the low surface-gravity and extreme youth of FFPs in Orion, together make the selection of bona-fide substellar objects quite challenging. The *Euclid* passbands are not specifically designed to distinguish FFPs from other types of objects. They are broader than the passbands commonly used in ground-based surveys because they include spectral regions affected by saturated telluric water absorption. The calibrations available for this ERO study are scarce. Improved calibrations are expected in the future when *Euclid* photometry and spectroscopy of benchmark ultracool dwarfs become available. We limit the scope of this work to present a high-purity approach to select objects using *Euclid* ERO catalogue and images that is anchored to the properties of the benchmarks described in the

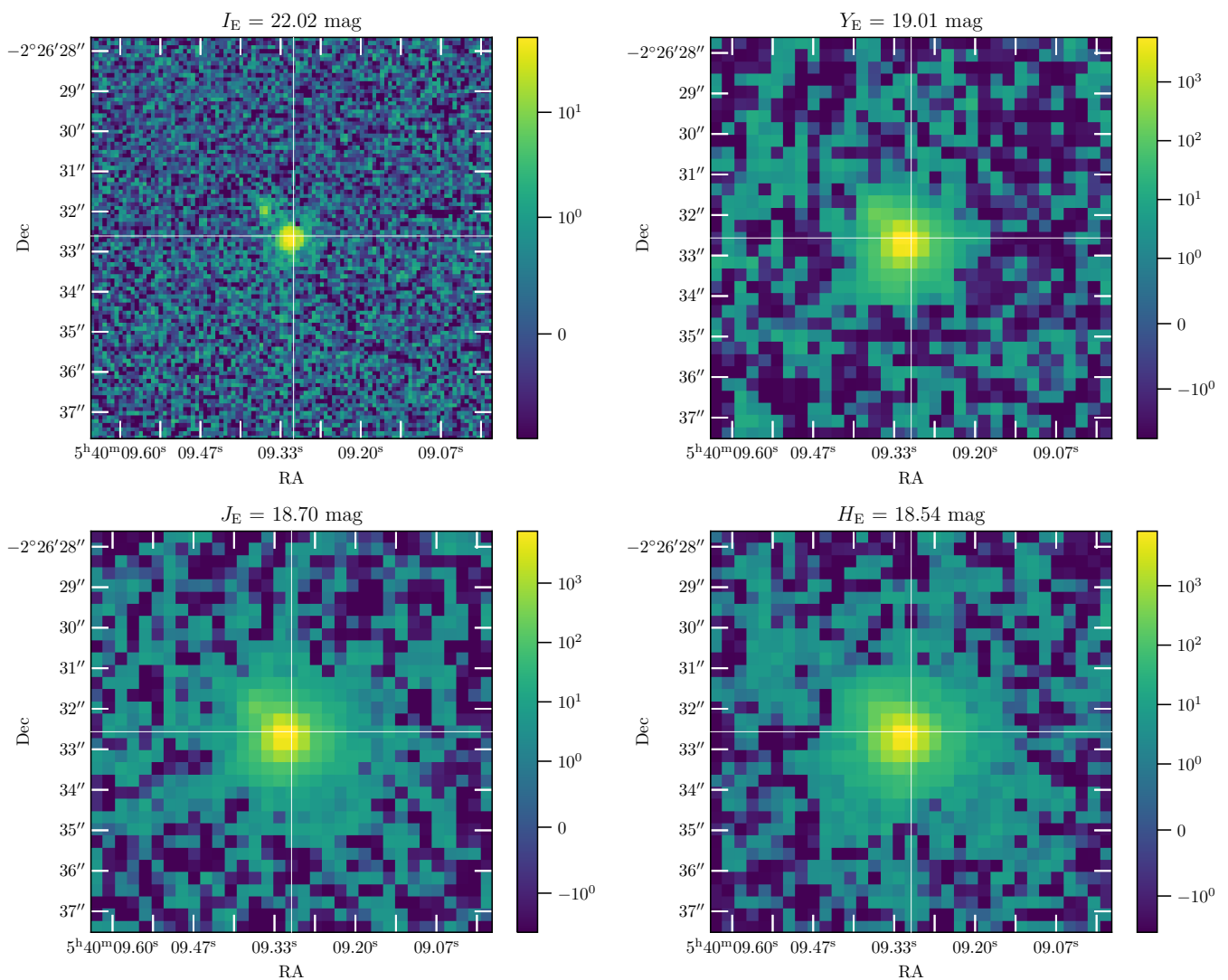


Fig. 3. Mosaic of *Euclid* images centred on the benchmark object S Ori 52 in the four different photometric passbands. We note the presence of a clearly resolved visual companion in the VIS image.

previous section. The selection cuts adopted in this work are presented in Table 4. To arrive at these selection cuts, we calculated the 1σ dispersion around the mean of the values for the benchmark sources and we added it to both extremes of the distribution.

The ERO-SOri photometric catalogue was filtered using the cuts provided in Table 4. The number of objects left after each step and the percentage with respect to the original sample are also given in the table. Note that the percentage of sources detected in the J_E band in the whole FoV adds up to 76.83% of the total number of sources in the ERO catalogue. Sources not detected in the J_E band have not been considered in this work because young substellar objects are expected to be much brighter in the J_E band than in the I_E band. The CLASS_STAR classifier was found to be redundant with the SPREAD_MODEL parameter, and the latter was chosen because the values for the benchmarks are more stable. The FoV was divided in two regions separated by a constant RA value of $85^{\circ}1875$. We call the low-reddening/dark-background part the σ Orionis region ($RA < 85^{\circ}1875$) and the high-reddening/bright-background part of the Horsehead region. We compared the distribution of SPREAD_MODEL_J between these two parts of the FoV and

found that it is narrower in the σ Orionis region than in the Horsehead region (Fig. 4). This is likely due to the influence of a brighter background on the Horsehead side owing to light reflected in the nebulosity. Thus, we consider that the cuts defined in this work are valid only for regions with low interstellar background and negligible extinction. For the regions affected by high sky background it will be important to obtain a new sample of substellar benchmarks using the *Euclid* NISP spectra.

4.3. Selection of new substellar member candidates in the σ Orionis cluster with *Euclid* data

After applying all the selection cuts defined above, only 2% of the sources in the initial catalogue remained. They are plotted in the I_E versus $I_E - J_E$ colour-magnitude diagram (CMD) following the approach of previous searches for substellar objects in the σ Orionis region (Peña Ramírez et al. 2012), and compared with the 3-Myr isochrone provided by the ATMO models of Phillips et al. (2020) that have been transformed into the *Euclid* photometric system for this work. These models have been tested using the dynamic lithium-boundary method for brown dwarf bi-

Table 2. *Euclid* parameters for σ Orionis benchmark objects. FWHM values are given in pixels.

Parameter	Object						
	S Ori 28	S Ori 52	S Ori 60	S Ori 62	S Ori 054017	S Ori 054000	S Ori 054037
SPREAD_MODEL_I	1.20×10^{-3}	-7.20×10^{-4}	3.14×10^{-4}	-7.06×10^{-4}	2.94×10^{-3}	1.82×10^{-3}	1.40×10^{-3}
SPREAD_MODEL_Y	1.24×10^{-2}	6.25×10^{-3}	6.96×10^{-6}	6.61×10^{-3}	7.24×10^{-3}	1.48×10^{-4}	-2.75×10^{-4}
SPREAD_MODEL_J	9.24×10^{-3}	3.37×10^{-4}	-1.59×10^{-3}	-2.14×10^{-3}	-5.83×10^{-3}	-1.59×10^{-4}	-3.76×10^{-3}
SPREAD_MODEL_H	6.80×10^{-3}	3.26×10^{-3}	3.74×10^{-3}	5.47×10^{-3}	-1.23×10^{-3}	-4.61×10^{-3}	1.10×10^{-2}
CLASS_STAR_I	0.98	1	0.81	0.86	0.68	0.76	0.75
CLASS_STAR_Y	0.99	1	1	0.92	0.98	0.98	1
CLASS_STAR_J	1	1	1	0.98	0.98	0.98	0.98
CLASS_STAR_H	1	1	1	0.94	0.98	0.98	0.97
FWHM_IMAGE_I	1.69	2.46	2.39	1.51	1.73	1.69	1.65
FWHM_IMAGE_Y	1.44	1.52	0.78	1.78	1.61	1.59	1.42
FWHM_IMAGE_J	1.83	1.54	0.8	1.46	1.29	1.66	1.37
FWHM_IMAGE_H	1.79	1.56	1.69	1.89	1.64	1.4	1.56
MAG_AUTO_I	18.4631	21.9735	23.7263	23.8577	24.9944	24.2328	24.3397
MAGERR_AUTO_I	0.0005	0.0048	0.023	0.0206	0.0537	0.0268	0.0305
MAG_AUTO_Y	16.3237	18.8565	20.597	20.5435	21.5509	20.8739	21.0935
MAGERR_AUTO_Y	0.001	0.0035	0.012	0.0118	0.0305	0.0215	0.0193
MAG_AUTO_J	16.3058	18.5677	20.1688	20.1503	21.0523	20.4058	20.6629
MAGERR_AUTO_J	0.0008	0.0023	0.0068	0.007	0.0162	0.0119	0.0111
MAG_AUTO_H	16.3073	18.3369	19.7774	19.8562	20.5806	20.0368	20.1653
MAGERR_AUTO_H	0.0008	0.002	0.0051	0.0055	0.0121	0.0089	0.0075
ELLIPTICITY_I	0.048	0.100	0.243	0.049	0.045	0.106	0.028
ELLIPTICITY_J	0.017	0.049	0.023	0.04	0.07	0.107	0.062

Table 3. Previously identified candidate members of the σ Orionis cluster not validated with *Euclid* data.

Name	RA	Dec	Comment
	[hh mm ss.ss]	[deg mm ss.s]	
S Ori 69	05 39 18.05	-02 28 54.1	extended
S Ori J053923-021235	05 39 23.28	-02 12 35.0	extended
S Ori J053929-024636	05 39 29.36	-02 46 37.1	high proper motion
S Ori 57	05 39 47.05	-02 25 24.5	high proper motion
S Ori J053956-025315	05 39 56.81	-02 53 14.6	extended
S Ori J054004-025332	05 40 04.48	-02 53 31.9	extended
PBZ12 J054011-025639	05 40 11.62	-02 56 39.4	high proper motion
S Ori J054014-025146	05 40 14.23	-02 51 46.3	extended
PBZ12 J054024-024444	05 40 24.32	-02 44 44.3	extended
PBZ12 J054025-024259	05 40 25.39	-02 42 59.7	extended
PBZ12 J054026-023100	05 40 26.44	-02 31 00.8	high proper motion
PBZ12 J054028-025116	05 40 27.99	-02 51 16.7	extended
PBZ12 J054038-022806	05 40 38.42	-02 28 06.6	extended

naries with dynamical masses and found to provide better fits to the observational data than other sets of models in the literature (Martín et al. 2022). The *Euclid* data and the CEQ (equilibrium chemistry) ATMO 3-Myr isochrone are shown in the CMD displayed in Fig. 5. The benchmarks clearly define the σ Orionis sequence, and other objects in the *Euclid* data that appear to follow this cluster sequence have been previously identified in the literature as photometric candidate members (Peña Ramírez et al. 2012). Their *Euclid* coordinates and photometry are provided in Table 5. Seven new objects were found to be located close to the cluster sequence and well separated from the cloud of background sources, including two very faint ones that extend the sequence to fainter magnitudes than previous surveys. The three brighter objects were retrieved in the VHS catalogue and

their coordinates were found to agree within 100 mas, so they do not have high proper motion. The coordinates and photometry of these seven new *Euclid* objects of interest identified in the σ Orionis cluster sequence are given in Table 6.

Further examination of the cluster sequence, its degree of agreement with the ATMO isochrone and the location of new candidate members was made in the colour-colour diagram shown in Fig. 6. The coolest benchmarks define a well separated locus away from the cloud of contaminating sources. The behaviour of the benchmarks is qualitatively fairly well reproduced by the isochrone, although quantitatively the fit could be improved because the isochrone does not reach as large $Y_E - H_E$ colour as observed. The blueing of the isochrone in the $Y_E - H_E$ colour beyond $I_E - Y_E \geq 3.5$ is an effect of the appearance of

Table 4. *Euclid* point-source selection criteria. The right ascension, RA, divides the two area into parts: the high-reddening region (RA < 85°1875); and the low reddening region (RA \geq 85°1875).

Cut No.	Criteria	High-reddening region		Low-reddening region	
		Count after cut	% of catalogue	Count after cut	% of catalogue
1	ra_J_E Cut	124 249	38.04	126 693	38.79
2	$-0.011 < \text{SPREAD_MODEL_J_E} < 0.014$	70 558	21.60	47 630	14.58
3	$0.472 < \text{FWHM_IMAGE_J_E} < 2.158$	24 174	7.40	14 932	4.57
4	$0 < \text{ELLIPTICITY_J_E} < 0.138$	17 423	5.33	10 742	3.29
5	$-0.01 < \text{SPREAD_MODEL_H_E} < 0.016$	14 574	4.81	7944	2.97
6	$1.238 < \text{FWHM_IMAGE_H_E} < 2.052$	12 262	3.87	7018	2.50
7	$-0.005 < \text{SPREAD_MODEL_Y_E} < 0.017$	11 550	3.62	6603	2.30
8	$0.461 < \text{FWHM_IMAGE_Y_E} < 2.099$	10 768	3.34	6208	2.03
9	Drop 99 in any I_E mag	9450	2.89	4663	1.43
10	$-0.002 < \text{SPREAD_MODEL_I_E} < 0.004$	6819	2.09	3445	1.05
11	$1.127 < \text{FWHM_IMAGE_I_E} < 2.843$	6614	2.03	3293	1.01

Table 5. *Euclid* photometry of previously-known non-benchmark objects in the σ Orionis cluster sequence.

RA (J2000)	Dec (J2000)	I_E	$\sigma(I_E)$	Y_E	$\sigma(Y_E)$	J_E	$\sigma(J_E)$	H_E	$\sigma(H_E)$
84°847 645	-2°682 660	20.445	0.002	17.812	0.002	17.583	0.001	17.508	0.001
84°872 332	-2°777 320	21.207	0.003	18.451	0.003	18.196	0.002	18.043	0.002
84°885 072	-2°872 183	24.299	0.027	20.923	0.016	20.547	0.009	20.055	0.006
84°943 614	-2°406 478	21.158	0.003	18.269	0.003	18.127	0.002	17.920	0.002
84°989 081	-2°835 013	23.618	0.016	20.300	0.011	20.028	0.007	19.749	0.006
85°028 991	-2°601 451	22.725	0.008	19.478	0.005	19.124	0.003	18.861	0.003
85°032 282	-2°376 239	23.945	0.022	20.758	0.017	20.284	0.009	19.915	0.007
85°076 609	-2°385 794	20.358	0.002	17.994	0.003	17.216	0.001	16.513	0.001
85°048 215	-2°859 726	24.400	0.039	21.159	0.017	20.872	0.011	20.705	0.010
84°919 110	-2°653 550	18.348	0.001	16.570	0.001	16.416	0.001	16.196	0.001
84°893 058	-2°646 380	18.266	0.001	15.986	0.001	15.967	0.001	15.882	0.001
84°815 680	-2°640 655	18.387	0.001	16.209	0.002	16.075	0.001	16.024	0.001
84°861 922	-2°615 620	18.952	0.001	16.585	0.001	16.452	0.001	16.414	0.001
85°018 897	-2°611 691	18.877	0.001	16.491	0.001	16.351	0.001	16.613	0.001
85°074 216	-2°448 392	19.842	0.002	17.473	0.002	17.312	0.001	17.164	0.001
85°142 016	-2°434 096	20.055	0.002	17.779	0.002	17.424	0.001	17.179	0.001
84°813 607	-2°364 092	19.135	0.001	16.728	0.002	16.615	0.002	16.525	0.002
84°808 099	-2°272 735	21.907	0.005	18.837	0.007	18.606	0.005	18.353	0.004

Table 6. *Euclid* objects of interest in the σ Orionis region.

Code	RA (J2000)	Dec (J2000)	I_E	$\sigma(I_E)$	Y_E	$\sigma(Y_E)$	J_E	$\sigma(J_E)$	H_E	$\sigma(H_E)$
A	85°162 830	-2°292 707	19.084	0.001	17.184	0.002	16.898	0.001	16.699	0.001
B	84°807 391	-2°529 354	21.692	0.007	18.724	0.006	18.523	0.004	18.361	0.004
C	85°036 499	-2°714 769	23.362	0.019	20.536	0.014	20.091	0.007	19.901	0.007
D	85°119 119	-2°851 646	23.779	0.025	20.545	0.011	20.211	0.007	19.840	0.005
E	84°892 801	-2°981 698	25.081	0.110	21.951	0.067	21.499	0.037	21.264	0.030
F	85°146 780	-2°918 538	26.444	0.194	22.897	0.095	22.670	0.061	22.286	0.042
G	84°818 225	-2°395 095	26.536	0.221	23.098	0.134	22.469	0.062	22.243	0.051

methane in the transition from L to T-type spectra. The new sources with codes D, E, and G fall within the L-type benchmark locus, making them strong FFP candidates. Source F is slightly bluer in $Y_E - H_E$ than the faintest benchmark, and is also closer to the isochrone, suggesting that it might be the first L/T transition FFP identified in the σ Orionis cluster. Confirmation of these tentative assessments requires spectroscopy.

To check the effects of reddening in the selection of substellar candidates, the same cuts that were applied to the σ Orionis region were also applied to the Horsehead regions. The CMD and colour-colour diagrams are shown in Figs. 7 and 8, respec-

tively. The separation between the cluster sequence defined by the benchmarks and the cloud of sources is no longer well defined in the CMD and the locus of benchmarks in the colour-colour diagram is not well isolated. This example shows the difficulties of selecting substellar candidates in regions with high interstellar reddening. Future work will address this issue.

To check for the presence of binaries, we show in Fig. 9 the FWHM values (in pixels) versus aperture magnitudes measured in the VIS images for all the objects under study (benchmarks, confirmed candidates in the cluster sequence, and new discoveries). Besides the two binary candidates among the benchmarks,

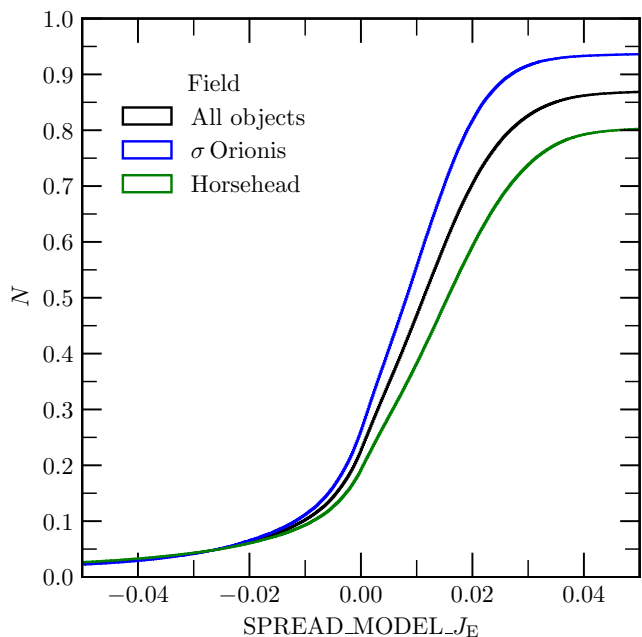


Fig. 4. Cumulative distribution of spread model values for the *Euclid* J_E band. The distribution of values in the low-reddening part corresponding to the σ Orionis cluster is sharper than in the high-reddening part.

there is one more candidate among the confirmed objects and one more among the new ones found with *Euclid*. The object labelled as G could be the first σ Orionis counterpart to the Jupiter-mass binary candidates reported in the Trapezium cluster (McCaughrean & Pearson 2023), but needs confirmation with higher spatial resolution images that could be provided by HST optical imaging observations.

5. The *Euclid* substellar IMF of the σ Orionis cluster

The results reported in this work are useful to revise the very low-mass IMF of the σ Orionis cluster and try to extend it deeper into the planetary-mass regime. The *Gaia* sample covers the domain of very low-mass stars and *Euclid* provides a continuation into the substellar-mass regime, reaching down to about $4 M_J$.

The mass-luminosity relationship from the 3-Myr ATMO CEQ models has been used for the substellar domain. The PADova and TRIeste Stellar Evolution Code (PARSEC) models (Bressan et al. 2012; Pastorelli et al. 2020) were used for the stellar domain. The IMF of the σ Orionis cluster using the *Gaia*-DR3 membership study by Žerjal et al. (2024), combined with the results of this work, is displayed in Fig. 10. Our results are consistent with a multi-power-law distribution for the IMF.

A comprehensive study of the IMF within a distance of 20 pc from the Sun has reported a change in the slope in the substellar domain (Kirkpatrick et al. 2024). Those authors claimed that the Solar vicinity IMF can be expressed as $dN/dM = C M^{-\alpha}$ with four different values of the power-law exponent for different mass intervals. In particular, in this work we are concerned with the low-mass tail of the IMF where the slope estimated by Kirkpatrick et al. (2024) steepens from a value of $\alpha = 0.25$ in the mass range $0.05 M_\odot < M < 0.22 M_\odot$ to $\alpha = 0.60$ in the mass range $0.01 M_\odot < M < 0.05 M_\odot$.

In this study, we identify three different mass regimes: the very low-mass stellar domain from 0.15 to $0.1 M_\odot$ with $\alpha =$

0.26 ± 0.10 ; the brown dwarf domain from 0.1 to $0.011 M_\odot$ with $\alpha = 0.18 \pm 0.01$; and the planetary-mass domain from 0.011 to $0.003 M_\odot$ with $\alpha = 0.12 \pm 0.02$. These values have been obtained with linear fits that are shown in Fig. 10. We excluded from the fits the mass range between $0.1 M_\odot$ and $0.05 M_\odot$ because those objects are too faint to be complete for *Gaia* and too bright for *Euclid*. Error bars quoted for the IMF slopes were estimated by simulations of the effects coming from age, distance and photometric uncertainties.

Our σ Orionis IMF results are consistent with the field in the very low-mass stellar regime and extend deeper into the substellar regime than the field IMF. We do not confirm a steepening of the substellar IMF at the planetary-mass end. These comparisons are affected by low number statistics. The census of directly imaged FFPs should be increased significantly to investigate the possibility of substellar IMF variations in different environments that could be an indication of specific formation pathways in the planetary-mass domain. These results demonstrate that *Euclid* can play a significant role in the detailed study of the low-mass shape of the IMF and particularly in shedding light on the formation mechanisms of FFPs. Detailed theoretical models developed by different groups have indicated that the shape of the IMF is a useful indicator of the dominant mode of star formation in a given region (Adams & Fatuzzo 1996; Chabrier 2005; Thies et al. 2015), and that a multi-power-law IMF could arise from the interplay between the mass-dependence and the time-dependence of exponential growth in a distribution of accreting protostars (Essex et al. 2020).

6. Final remarks: The impact of *Euclid* on the study of FFPs in star-forming regions

This work is a showcase of the power of the *Euclid* mission to provide the area and depth required to explore the very low-mass population, including FFPs of nearby star-forming regions and very young open clusters. In particular, for the well-known σ Orionis cluster, we show that the sensitivity of the *Euclid* images is capable of probing down to FFPs that could have masses as low as $4 M_J$ according to theoretical models (for 3 Myr ages) and at a distance of 400 pc. This potential could be compromised by severe contamination from numerous background extragalactic sources if we do not use stringent selection procedures. Using the *Euclid* data for seven benchmark objects in σ Orionis, we have developed a high-purity method to filter out the contamination. This method is valid for regions of low reddening, but it needs additional work to be generalised to regions with any reddening. We note that the *Euclid* NISP spectra will likely play an important role in this effort. Additionally multi-epoch observations with *Euclid* during the lifetime of the mission, possibly filling gaps in the cosmological surveys, can enable the study of proper motions and photometric variability that are useful probes for the study of the low-mass population in star-forming regions.

This is the first of a series of papers that intend to explore several star-forming regions using *Euclid* observations. The observations presented here provide a glimpse of the power of *Euclid* to shed light on the long-standing question of the putative low-mass cutoff of the IMF predicted long time ago by the theory of opacity-limited fragmentation and collapse of molecular clouds. Our IMF for the σ Orionis open cluster extends previous studies to lower planetary masses and suggests that there could be a difference in slope in the substellar regime between this young open cluster and the field, hinting at a possible sensitivity to environmental conditions. This study demonstrates the great

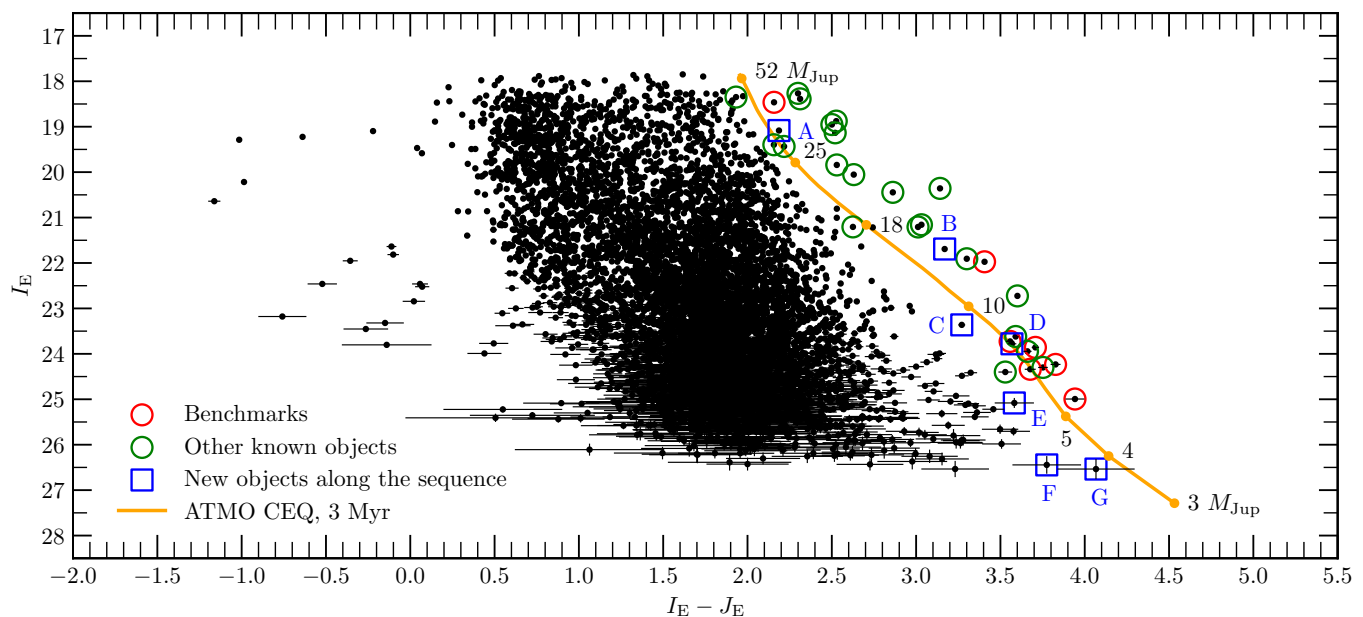


Fig. 5. The I_E versus $I_E - J_E$ colour-magnitude diagram for the σ Orionis part of the FoV. Black points are all the *Euclid* sources that remain after applying all the cuts. Benchmark objects are denoted with red circles. New objects near the cluster sequence are denoted with blue squares and labelled with capital letters. Known sources, other than the benchmarks, in the σ Orionis cluster are denoted with green circles. An ATMO CEQ isochrone (see Phillips et al. 2020) for an age of 3 Myr and a distance of 402.74 pc is shown. Theoretical masses are labelled on the isochrone.

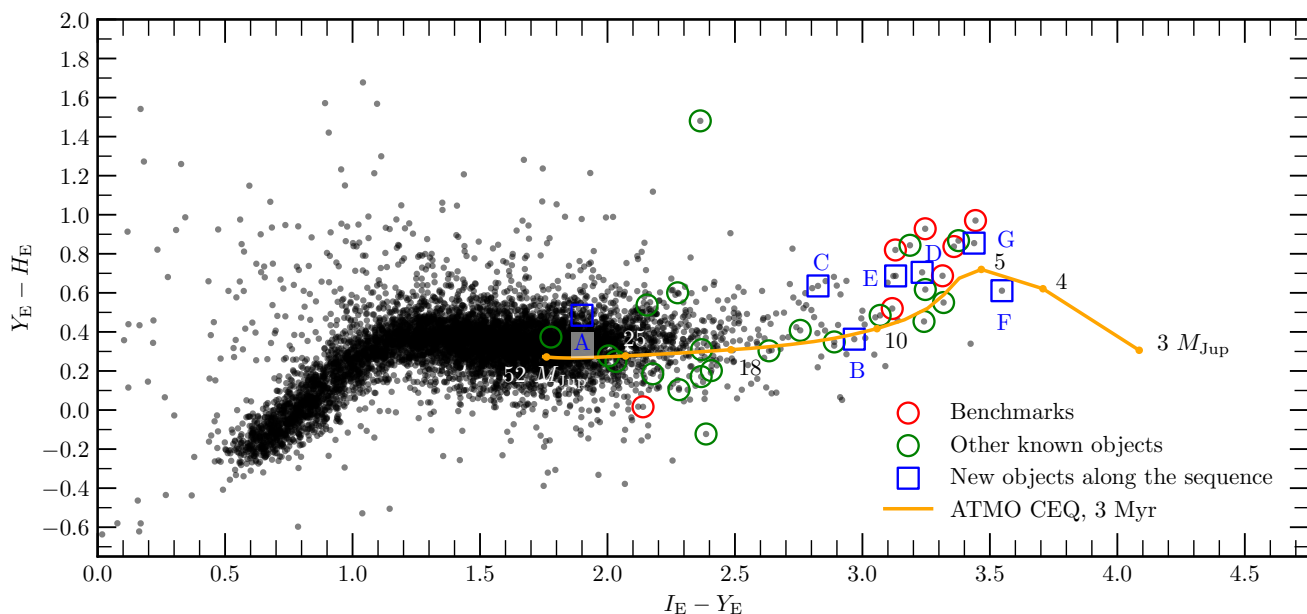


Fig. 6. The $I_E - Y_E$ versus $Y_E - H_E$ colour-colour diagram for the same region as the previous figure (σ Orionis). All the symbols remain the same.

potential of *Euclid* to tackle the study of the substellar IMF in nearby star-forming regions and very young open clusters.

Acknowledgements. This work has made use of the Early Release Observations (ERO) data from the *Euclid* mission of the European Space Agency (ESA), 2024. We thank I. Baraffe and M. Phillips for making available a digitised version of their isochrones in the *Euclid* passbands. E.L.M. and M.Ž. are supported by the European Research Council Advanced grant SUBSTELLAR, project number 101054354. This research has made use of the Spanish Virtual Observatory (<https://svo.cab.inta-csic.es>) project funded by MCIN/AEI/10.13039/501100011033/ through grant PID2020-112949GB-I00 at Centro de Astrobiología (CSIC-INTA). DB and NH have been supported by PID2019-107061GB-C61 by the same agency. P.M.B. is funded by Instituto Na-

cional de Técnica Aeroespacial through grant PRE-OVE. P.C. acknowledges financial support from the Spanish Virtual Observatory project (grant PID2020-112949GB-I00). N.P.B. is funded by Vietnam National Foundation for Science and Technology Development (NAFOSTED) under grant number 103.99-2020.63. NL and VJSB acknowledge financial support from the Agencia Estatal de Investigación (AEI/10.13039/501100011033) of the Ministerio de Ciencia e Innovación and the ERDF ‘A way of making Europe’ through project PID2022-137241NB-C1. CdB acknowledges support from a Beatriz Galindo senior fellowship (BG22/00166) from the Spanish Ministry of Science, Innovation and Universities. The *Euclid* Consortium acknowledges the European Space Agency and a number of agencies and institutes that have supported the development of *Euclid*, in particular the Agenzia Spaziale Italiana, the Austrian Forschungsförderungsgesellschaft funded through BMK, the Belgian Science Policy, the

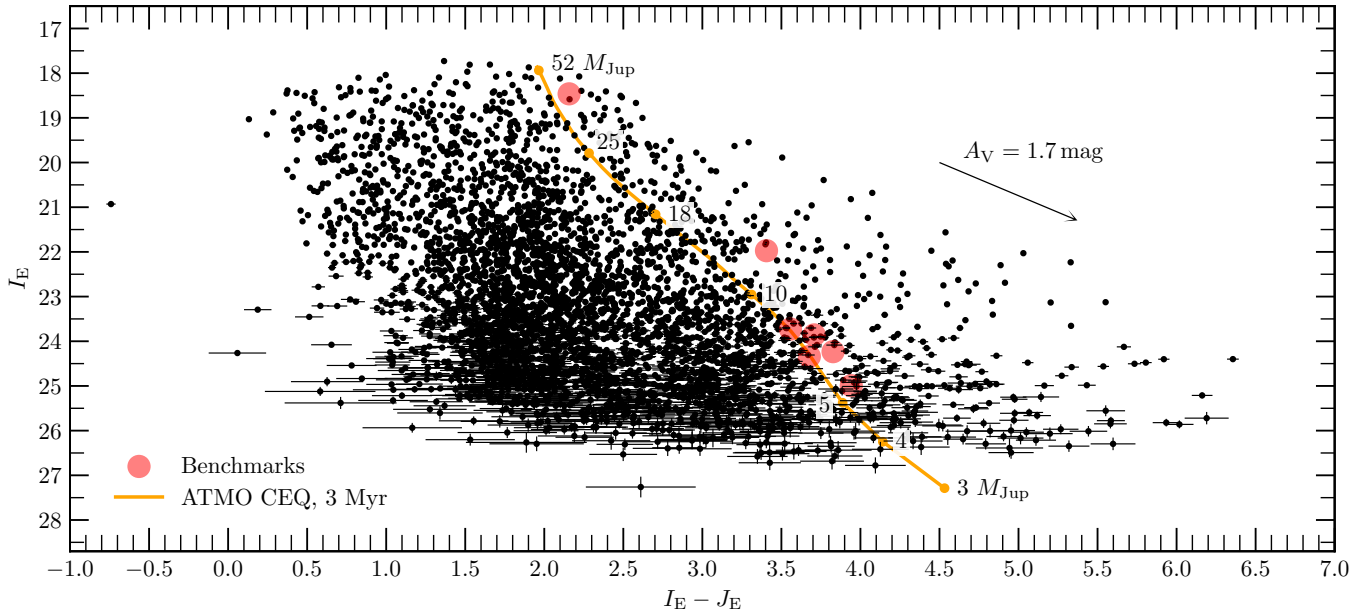


Fig. 7. The I_E versus $I_E - J_E$ colour-magnitude diagram for the Horsehead part of the FoV (not σ Orionis). The σ Orionis benchmarks are denoted with red circles. A reddening vector is shown as an arrow.

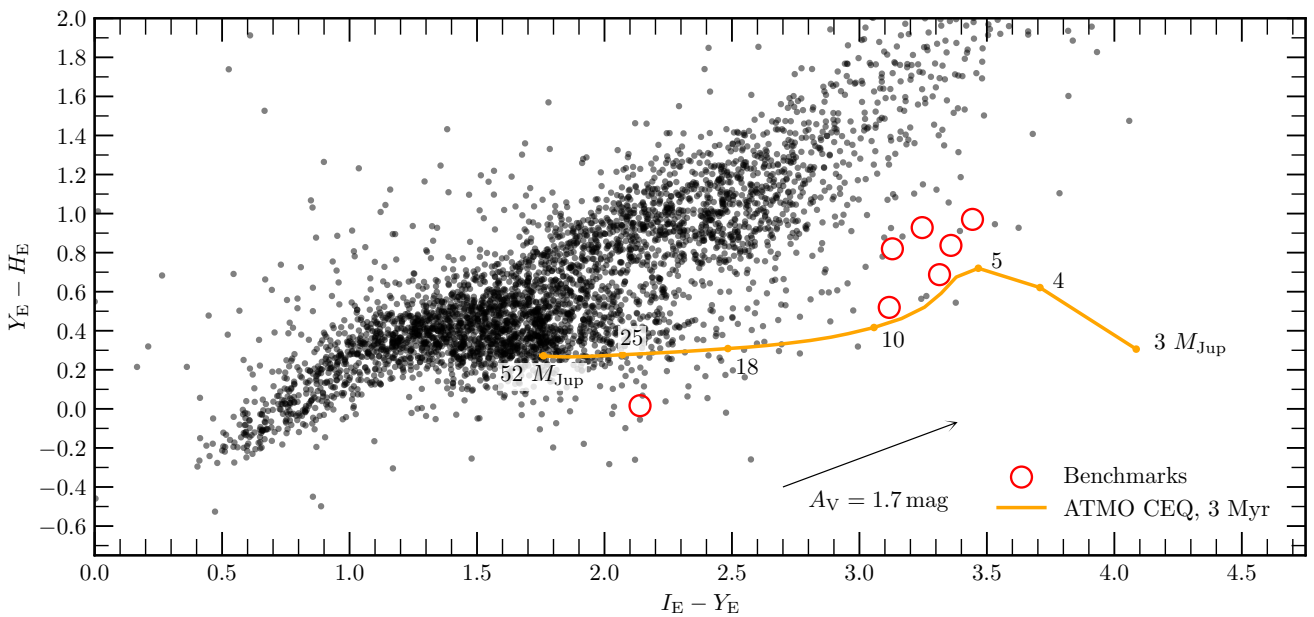


Fig. 8. The $I_E - Y_E$ versus $Y_E - H_E$ colour-colour diagram for the Horsehead part of the FoV (not σ Orionis). The σ Orionis benchmarks are denoted with red circles. A reddening vector is shown as an arrow.

Canadian Euclid Consortium, the Deutsches Zentrum für Luft- und Raumfahrt, the DTU Space and the Niels Bohr Institute in Denmark, the French Centre National d'Études Spatiales, the Fundação para a Ciência e a Tecnologia, the Hungarian Academy of Sciences, the Ministerio de Ciencia, Innovación y Universidades, the National Aeronautics and Space Administration, the National Astronomical Observatory of Japan, the Nederlandse Onderzoekschool Voor Astronomie, the Norwegian Space Agency, the Research Council of Finland, the Romanian Space Agency, the State Secretariat for Education, Research, and Innovation (SERI) at the Swiss Space Office (SSO), and the United Kingdom Space Agency. A complete and detailed list is available on the *Euclid* web site (<http://www.euclid-ec.org>).

References

- Adams, F. C. & Fatuzzo, M. 1996, *ApJ*, 464, 256
 Bally, J., Chambers, E., Guzman, V., et al. 2018, *AJ*, 155, 80
 Barrado y Navascués, D., Zapatero Osorio, M. R., Béjar, V. J. S., et al. 2001, *A&A*, 377, L9
 Bayo, A., Barrado, D., Stauffer, J., et al. 2011, *A&A*, 536, A63
 Béjar, V. J. S., Martín, E. L., Zapatero Osorio, M. R., et al. 2001, *ApJ*, 556, 830
 Bodenheimer, P. 1966, *ApJ*, 144, 103
 Bouy, H., Bertin, E., Moraux, E., et al. 2013, *A&A*, 554, A101
 Bouy, H., Tamura, M., Barrado, D., et al. 2022, *A&A*, 664, A111
 Bressan, A., Marigo, P., Girardi, L., et al. 2012, *MNRAS*, 427, 127
 Chabrier, G. 2005, in *Astrophysics and Space Science Library*, Vol. 327, The Initial Mass Function 50 Years Later, ed. E. Corbelli, F. Palla, & H. Zinnecker, 41

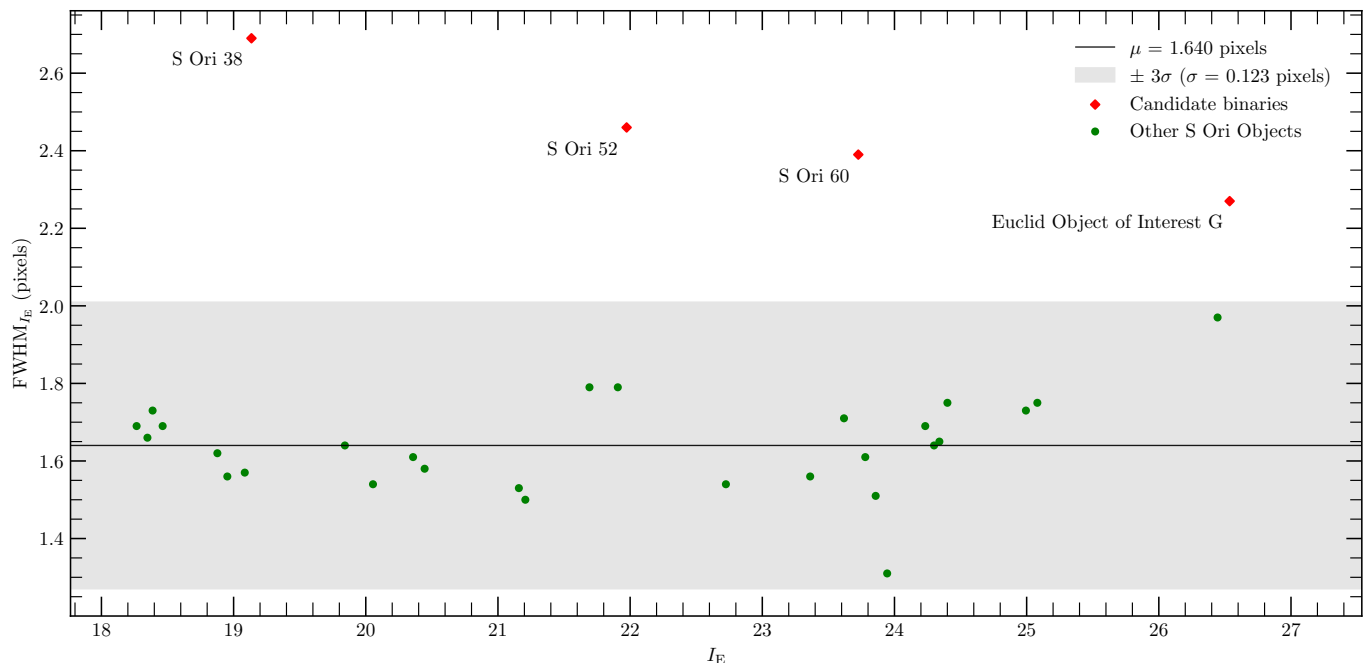


Fig. 9. FWHM (in pixels) versus I_E apparent magnitude (aperture photometry) for objects confirmed by *Euclid* to be in the σ Orionis cluster sequence. Both the FWHM and I_E photometry values come from the ERO catalogue and were measured in the *Euclid* VIS images. Four objects were found to have FWHM values larger than the mean value of cluster members (more than 3σ significance) and hence are considered as possible binaries that deserve further scrutiny. Two of them are benchmark objects, namely (S Ori 52 and S Ori 60), one is a known object (S Ori 38), and the faintest one is a new discovery (*Euclid* object of interest G).

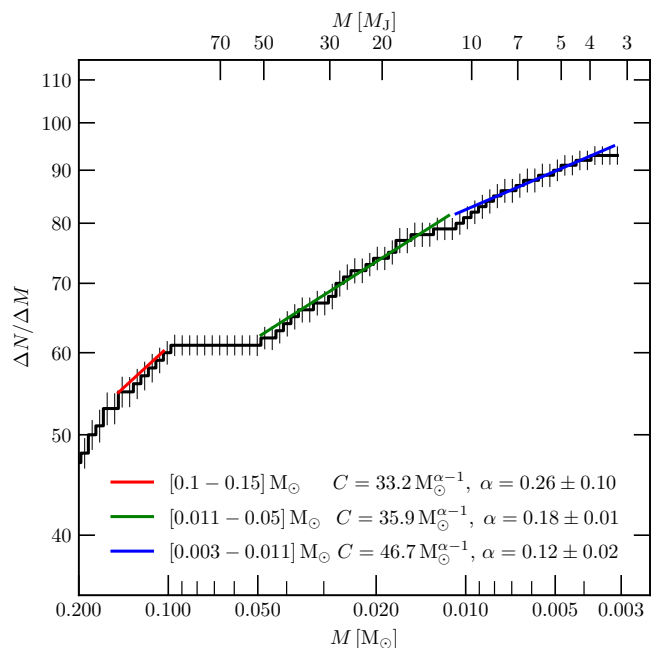


Fig. 10. Combined very low-mass *Euclid-Gaia* IMF of the σ Orionis cluster with linear fits in three different mass regions.

Chabrier, G., Baraffe, I., Allard, F., & Hauschildt, P. 2000, *ApJ*, 542, L119
 Chauvin, G., Lagrange, A. M., Dumas, C., et al. 2005, *A&A*, 438, L25
 Chiang, P. & Chen, W. P. 2015, *ApJ*, 811, L16
 Cuillandre, J.-C., Bertin, E., Bolzonella, M., et al. 2024, *A&A*, this issue
 Damian, B., Jose, J., Biller, B., et al. 2023, *ApJ*, 951, 139
 Depoy, D. L., Lada, E. A., Gatley, I., & Probst, R. 1990, *ApJ*, 356, L55
 Esplin, T. L. & Luhman, K. L. 2017, *AJ*, 154, 134

Esplin, T. L. & Luhman, K. L. 2019, *AJ*, 158, 54
 Essex, C., Basu, S., Prehl, J., & Hoffmann, K. H. 2020, *MNRAS*, 494, 1579
 Euclid Collaboration: Cropper, M., Al Bahlawan, A., Amiaux, J., et al. 2024, *A&A*, this issue
 Euclid Collaboration: Jahnke, K., Gillard, W., Schirmer, M., et al. 2024, *A&A*, this issue
 Euclid Collaboration: Mellier, Y., Abdurro'uf, Acevedo Barroso, J., Achúcarro, A., et al. 2024, *A&A*, this issue
 Euclid Collaboration: Scaramella, R., Amiaux, J., Mellier, Y., et al. 2022, *A&A*, 662, A112
 Euclid Early Release Observations. 2024, <https://doi.org/10.57780/esa-qmocz3>
 Gaia Collaboration, Vallenari, A., Brown, A. G. A., et al. 2023, *A&A*, 674, A1
 Gauza, B., Béjar, V. J. S., Pérez-Garrido, A., et al. 2015, *ApJ*, 804, 96
 Green, G. M. 2018, *The Journal of Open Source Software*, 3, 695
 Green, G. M., Schlafly, E., Zucker, C., Speagle, J. S., & Finkbeiner, D. 2019, *ApJ*, 887, 93
 Hennebelle, P. & Chabrier, G. 2008, *ApJ*, 684, 395
 Hunt, L., Annibali, F., Cuillandre, J.-C., et al. 2024, *A&A*, this issue
 Jun-Yan Zhang, J., Lodieu, N., & Martín, E. 2024, *arXiv e-prints*, arXiv:2403.15288
 Kirkpatrick, J. D., Marocco, F., Gelino, C. R., et al. 2024, *ApJS*, 271, 55
 Kluge, M., Hatch, N., Montes, M., et al. 2024, *A&A*, this issue
 Koshimoto, N., Sumi, T., Bennett, D. P., et al. 2023, *AJ*, 166, 107
 Kounkel, M., Hartmann, L., Mateo, M., & Bailey, John I., I. 2017, *ApJ*, 844, 138
 Kounkel, M., Megeath, S. T., Poteet, C. A., Fischer, W. J., & Hartmann, L. 2016, *ApJ*, 821, 52
 Langeroodi, D. & Hjorth, J. 2023, *ApJ*, 957, L27
 Laureijs, R., Amiaux, J., Arduini, S., et al. 2011, *ESA/SRE(2011)12*, arXiv:1110.3193
 Lodieu, N., Hambly, N. C., & Cross, N. J. G. 2021, *MNRAS*, 503, 2265
 Lodieu, N., Zapatero Osorio, M. R., Béjar, V. J. S., & Peña Ramírez, K. 2018, *MNRAS*, 473, 2020
 Lodieu, N., Zapatero Osorio, M. R., Rebolo, R., Martín, E. L., & Hambly, N. C. 2009, *A&A*, 505, 1115
 Lucas, P. W. & Roche, P. F. 2000, *MNRAS*, 314, 858
 Lucas, P. W., Roche, P. F., Allard, F., & Hauschildt, P. H. 2001, *MNRAS*, 326, 695
 Lucas, P. W., Weights, D. J., Roche, P. F., & Riddick, F. C. 2006, *MNRAS*, 373, L60
 Luhman, K. L., Peterson, D. E., & Megeath, S. T. 2004, *ApJ*, 617, 565

- Marleau, F., Cuillandre, J.-C., Cantiello, M., et al. 2024, A&A, this issue
- Martín, E. L., Barrado y Navascués, D., Baraffe, I., Bouy, H., & Dahm, S. 2003, *ApJ*, 594, 525
- Martin, E. L., Bouy, H., Martin, D., et al. 2023, *Proc.*, 30th Rencontres du Vietnam: Windows on the Universe
- Martín, E. L., Lodieu, N., & del Burgo, C. 2022, *MNRAS*, 510, 2841
- Martín, E. L., Zapatero Osorio, M. R., Barrado y Navascués, D., Béjar, V. J. S., & Rebolo, R. 2001, *ApJ*, 558, L117
- Martín, E. L., Zhang, J. Y., Esparza, P., et al. 2021, A&A, 655, L3
- Massari, D., Dalessandro, E., Erkal, D., et al. 2024, A&A, this issue
- McCaughrean, M. J. & Pearson, S. G. 2023, arXiv e-prints, arXiv:2310.03552
- McMahon, R. G., Banerji, M., Gonzalez, E., et al. 2021, *VizieR Online Data Catalog*, II/367
- Miret-Roig, N. 2023, *Ap&SS*, 368, 17
- Miret-Roig, N., Bouy, H., Raymond, S. N., et al. 2022, *Nat. Astron.*, 6, 89
- Mohr, J. J., Armstrong, R., Bertin, E., et al. 2012, in *SPIE Conf. Ser.*, Vol. 8451, Software and Cyberinfrastructure for Astronomy II, ed. N. M. Radziwill & G. Chiozzi, 84510D
- Mondal, A. & Chattopadhyay, T. 2019, *New A*, 66, 45
- Mookerjea, B., Sandell, G., Jarrett, T. H., & McMullin, J. P. 2009, A&A, 507, 1485
- Mroz, P., Ryu, Y. H., Skowron, J., et al. 2018, *AJ*, 155, 121
- Oasa, Y., Tamura, M., & Sugitani, K. 1999, *ApJ*, 526, 336
- Olivares, J., Bouy, H., Sarro, L. M., et al. 2021, A&A, 649, A159
- Padoan, P. & Nordlund, Å. 2004, *ApJ*, 617, 559
- Pastorelli, G., Marigo, P., Girardi, L., et al. 2020, *MNRAS*, 498, 3283
- Peña Ramírez, K., Béjar, V. J. S., Zapatero Osorio, M. R., Petr-Gotzens, M. G., & Martín, E. L. 2012, *ApJ*, 754, 30
- Phillips, M. W., Tremblin, P., Baraffe, I., et al. 2020, A&A, 637, A38
- Planck Collaboration. 2016, A&A, 596, A109
- Saifollahi, T., Voggel, K., Lançon, A., et al. 2024, A&A, this issue
- Salpeter, E. E. 1955, *ApJ*, 121, 161
- Scholz, A., Muzic, K., Jayawardhana, R., Almodros-Abad, V., & Wilson, I. 2023, *AJ*, 165, 196
- Silk, J. 1977, *ApJ*, 214, 152
- Solano, E., Gálvez-Ortiz, M. C., Martín, E. L., et al. 2021, *MNRAS*, 501, 281
- Spezzi, L., Petr-Gotzens, M. G., Alcalá, J. M., et al. 2015, A&A, 581, A140
- Stahler, S. W. 1988, *ApJ*, 332, 804
- Sumi, T., Koshimoto, N., Bennett, D. P., et al. 2023, *AJ*, 166, 108
- Thies, I., Pflamm-Altenburg, J., Kroupa, P., & Marks, M. 2015, *ApJ*, 800, 72
- Zerjal, M., Martín, E. L., & Pérez Garrido, A. 2024, A&A, in press
- Walter, F. M., Sherry, W. H., Wolk, S. J., & Adams, N. R. 2008, in *Handbook of Star Forming Regions, Volume I*, ed. B. Reipurth, Vol. 4 (ASP Conf. Ser.), 732
- Weaver, J., Taamoli, S., McPartland, C., et al. 2024, A&A, this issue
- Zapatero Osorio, M. R., Béjar, V. J. S., Martín, E. L., et al. 2000, *Science*, 290, 103
- Zapatero Osorio, M. R., Béjar, V. J. S., Pavlenko, Y., et al. 2002, A&A, 384, 937
- Zapatero Osorio, M. R., Béjar, V. J. S., & Peña Ramírez, K. 2017, *ApJ*, 842, 65
- Zhang, Z., Liu, M. C., Best, W. M. J., Dupuy, T. J., & Siverd, R. J. 2021, *ApJ*, 911, 7
- ¹¹ Observatoire Astronomique de Strasbourg (ObAS), Université de Strasbourg - CNRS, UMR 7550, Strasbourg, France
- ¹² Kapteyn Astronomical Institute, University of Groningen, PO Box 800, 9700 AV Groningen, The Netherlands
- ¹³ Université Paris-Saclay, Université Paris Cité, CEA, CNRS, AIM, 91191, Gif-sur-Yvette, France
- ¹⁴ Max-Planck-Institut für Astronomie, Königstuhl 17, 69117 Heidelberg, Germany
- ¹⁵ Ohio University, Physics & Astronomy Department, 1 Ohio University, Athens, OH 45701, USA
- ¹⁶ NSF's NOIR, Lab 950 N. Cherry Avenue, Tucson, Arizona 85719, USA
- ¹⁷ Department of Physics, International University, Ho Chi Minh City, Vietnam
- ¹⁸ Vietnam National University, Ho Chi Minh City, Vietnam
- ¹⁹ International Space University, 1 rue Jean-Dominique Cassini, 67400 Illkirch-Graffenstaden, France
- ²⁰ School of Physics and Astronomy, University of Leicester, University Road, Leicester, LE1 7RH, UK
- ²¹ Université de Franche-Comté, Institut UTINAM, CNRS UMR6213, OSU THETA Franche-Comté-Bourgogne, Observatoire de Besançon, BP 1615, 25010 Besançon Cedex, France
- ²² INAF-Osservatorio Astrofisico di Torino, Via Osservatorio 20, 10025 Pino Torinese (TO), Italy
- ²³ School of Physics, Astronomy and Mathematics, University of Hertfordshire, College Lane, Hatfield AL10 9AB, UK
- ²⁴ Université Paris-Saclay, CNRS, Institut d'astrophysique spatiale, 91405, Orsay, France
- ²⁵ ESAC/ESA, Camino Bajo del Castillo, s/n., Urb. Villafranca del Castillo, 28692 Villanueva de la Cañada, Madrid, Spain
- ²⁶ INAF-Osservatorio Astronomico di Brera, Via Brera 28, 20122 Milano, Italy
- ²⁷ INAF-Osservatorio di Astrofisica e Scienza dello Spazio di Bologna, Via Piero Gobetti 93/3, 40129 Bologna, Italy
- ²⁸ Dipartimento di Fisica e Astronomia, Università di Bologna, Via Gobetti 93/2, 40129 Bologna, Italy
- ²⁹ INFN-Sezione di Bologna, Viale Berti Pichat 6/2, 40127 Bologna, Italy
- ³⁰ INAF-Osservatorio Astronomico di Padova, Via dell'Osservatorio 5, 35122 Padova, Italy
- ³¹ Centre National d'Etudes Spatiales – Centre spatial de Toulouse, 18 avenue Edouard Belin, 31401 Toulouse Cedex 9, France
- ³² Max Planck Institute for Extraterrestrial Physics, Giessenbachstr. 1, 85748 Garching, Germany
- ³³ Universitäts-Sternwarte München, Fakultät für Physik, Ludwig-Maximilians-Universität München, Scheinerstrasse 1, 81679 München, Germany
- ³⁴ Dipartimento di Fisica, Università di Genova, Via Dodecaneso 33, 16146, Genova, Italy
- ³⁵ INFN-Sezione di Genova, Via Dodecaneso 33, 16146, Genova, Italy
- ³⁶ Department of Physics "E. Pancini", University Federico II, Via Cinthia 6, 80126, Napoli, Italy
- ³⁷ INAF-Osservatorio Astronomico di Capodimonte, Via Moiarriello 16, 80131 Napoli, Italy
- ³⁸ INFN section of Naples, Via Cinthia 6, 80126, Napoli, Italy
- ³⁹ Instituto de Astrofísica e Ciências do Espaço, Universidade do Porto, CAUP, Rua das Estrelas, PT4150-762 Porto, Portugal
- ⁴⁰ Dipartimento di Fisica, Università degli Studi di Torino, Via P. Giuria 1, 10125 Torino, Italy
- ⁴¹ INFN-Sezione di Torino, Via P. Giuria 1, 10125 Torino, Italy
- ⁴² INAF-IASF Milano, Via Alfonso Corti 12, 20133 Milano, Italy
- ⁴³ Centro de Investigaciones Energéticas, Medioambientales y Tecnológicas (CIEMAT), Avenida Complutense 40, 28040 Madrid, Spain
- ⁴⁴ Port d'Informació Científica, Campus UAB, C. Albareda s/n, 08193 Bellaterra (Barcelona), Spain
- ⁴⁵ Institute for Theoretical Particle Physics and Cosmology (TTK), RWTH Aachen University, 52056 Aachen, Germany
- ¹ Instituto de Astrofísica de Canarias, Calle Vía Láctea s/n, 38204, San Cristóbal de La Laguna, Tenerife, Spain
- ² Departamento de Astrofísica, Universidad de La Laguna, 38206, La Laguna, Tenerife, Spain
- ³ Laboratoire d'Astrophysique de Bordeaux, CNRS and Université de Bordeaux, Allée Geoffroy St. Hilaire, 33165 Pessac, France
- ⁴ Institut universitaire de France (IUF), 1 rue Descartes, 75231 PARIS CEDEX 05, France
- ⁵ Departamento de Física Fundamental. Universidad de Salamanca. Plaza de la Merced s/n. 37008 Salamanca, Spain
- ⁶ Centro de Astrobiología (CAB), CSIC-INTA, ESAC Campus, Camino Bajo del Castillo s/n, 28692 Villanueva de la Cañada, Madrid, Spain
- ⁷ Departamento de Inteligencia Artificial, Universidad Nacional de Educación a Distancia (UNED), c/Juan del Rosal 16, E-28040, Madrid, Spain
- ⁸ Departamento Física Aplicada, Universidad Politécnica de Cartagena, Campus Muralla del Mar, 30202 Cartagena, Murcia, Spain
- ⁹ European Space Agency/ESTEC, Keplerlaan 1, 2201 AZ Noordwijk, The Netherlands
- ¹⁰ Aurora Technology for European Space Agency (ESA), Camino bajo del Castillo, s/n, Urbanizacion Villafranca del Castillo, Villanueva de la Cañada, 28692 Madrid, Spain

- ⁴⁶ INAF-Osservatorio Astronomico di Roma, Via Frascati 33, 00078 Monteporzio Catone, Italy
- ⁴⁷ Dipartimento di Fisica e Astronomia "Augusto Righi" - Alma Mater Studiorum Università di Bologna, Viale Berti Pichat 6/2, 40127 Bologna, Italy
- ⁴⁸ Institute for Astronomy, University of Edinburgh, Royal Observatory, Blackford Hill, Edinburgh EH9 3HJ, UK
- ⁴⁹ Jodrell Bank Centre for Astrophysics, Department of Physics and Astronomy, University of Manchester, Oxford Road, Manchester M13 9PL, UK
- ⁵⁰ European Space Agency/ESRIN, Largo Galileo Galilei 1, 00044 Frascati, Roma, Italy
- ⁵¹ Université Claude Bernard Lyon 1, CNRS/IN2P3, IP2I Lyon, UMR 5822, Villeurbanne, F-69100, France
- ⁵² Institute of Physics, Laboratory of Astrophysics, Ecole Polytechnique Fédérale de Lausanne (EPFL), Observatoire de Sauverny, 1290 Versoix, Switzerland
- ⁵³ UCB Lyon 1, CNRS/IN2P3, IUF, IP2I Lyon, 4 rue Enrico Fermi, 69622 Villeurbanne, France
- ⁵⁴ Mullard Space Science Laboratory, University College London, Holmbury St Mary, Dorking, Surrey RH5 6NT, UK
- ⁵⁵ Departamento de Física, Faculdade de Ciências, Universidade de Lisboa, Edifício C8, Campo Grande, PT1749-016 Lisboa, Portugal
- ⁵⁶ Instituto de Astrofísica e Ciências do Espaço, Faculdade de Ciências, Universidade de Lisboa, Campo Grande, 1749-016 Lisboa, Portugal
- ⁵⁷ Department of Astronomy, University of Geneva, ch. d'Ecogia 16, 1290 Versoix, Switzerland
- ⁵⁸ INAF-Istituto di Astrofisica e Planetologia Spaziali, via del Cavaliere, 100, 00100 Roma, Italy
- ⁵⁹ INFN-Padova, Via Marzolo 8, 35131 Padova, Italy
- ⁶⁰ Institut d'Estudis Espacials de Catalunya (IEEC), Edifici RDIT, Campus UPC, 08860 Castelldefels, Barcelona, Spain
- ⁶¹ Institut de Ciències de l'Espai (IEEC-CSIC), Campus UAB, Carrer de Can Magrans, s/n Cerdanyola del Vallés, 08193 Barcelona, Spain
- ⁶² INAF-Osservatorio Astronomico di Trieste, Via G. B. Tiepolo 11, 34143 Trieste, Italy
- ⁶³ Aix-Marseille Université, CNRS/IN2P3, CPPM, Marseille, France
- ⁶⁴ Istituto Nazionale di Fisica Nucleare, Sezione di Bologna, Via Irnerio 46, 40126 Bologna, Italy
- ⁶⁵ FRACTAL S.L.N.E., calle Tulipán 2, Portal 13 1A, 28231, Las Rozas de Madrid, Spain
- ⁶⁶ Dipartimento di Fisica "Aldo Pontremoli", Università degli Studi di Milano, Via Celoria 16, 20133 Milano, Italy
- ⁶⁷ Institute of Theoretical Astrophysics, University of Oslo, P.O. Box 1029 Blindern, 0315 Oslo, Norway
- ⁶⁸ Leiden Observatory, Leiden University, Einsteinweg 55, 2333 CC Leiden, The Netherlands
- ⁶⁹ Jet Propulsion Laboratory, California Institute of Technology, 4800 Oak Grove Drive, Pasadena, CA, 91109, USA
- ⁷⁰ Department of Physics, Lancaster University, Lancaster, LA1 4YB, UK
- ⁷¹ Felix Hormuth Engineering, Goethestr. 17, 69181 Leimen, Germany
- ⁷² Technical University of Denmark, Elektrovej 327, 2800 Kgs. Lyngby, Denmark
- ⁷³ Cosmic Dawn Center (DAWN), Denmark
- ⁷⁴ Institut d'Astrophysique de Paris, UMR 7095, CNRS, and Sorbonne Université, 98 bis boulevard Arago, 75014 Paris, France
- ⁷⁵ NASA Goddard Space Flight Center, Greenbelt, MD 20771, USA
- ⁷⁶ Department of Physics and Helsinki Institute of Physics, Gustaf Hällströmin katu 2, 00014 University of Helsinki, Finland
- ⁷⁷ AIM, CEA, CNRS, Université Paris-Saclay, Université de Paris, 91191 Gif-sur-Yvette, France
- ⁷⁸ Université de Genève, Département de Physique Théorique and Centre for Astroparticle Physics, 24 quai Ernest-Ansermet, CH-1211 Genève 4, Switzerland
- ⁷⁹ Department of Physics, P.O. Box 64, 00014 University of Helsinki, Finland
- ⁸⁰ Helsinki Institute of Physics, Gustaf Hällströmin katu 2, University of Helsinki, Helsinki, Finland
- ⁸¹ Aix-Marseille Université, CNRS, LAM, Marseille, France
- ⁸² NOVA optical infrared instrumentation group at ASTRON, Oude Hoogeveensedijk 4, 7991PD, Dwingeloo, The Netherlands
- ⁸³ INFN-Sezione di Milano, Via Celoria 16, 20133 Milano, Italy
- ⁸⁴ Universität Bonn, Argelander-Institut für Astronomie, Auf dem Hügel 71, 53121 Bonn, Germany
- ⁸⁵ Dipartimento di Fisica e Astronomia "Augusto Righi" - Alma Mater Studiorum Università di Bologna, via Piero Gobetti 93/2, 40129 Bologna, Italy
- ⁸⁶ Department of Physics, Centre for Extragalactic Astronomy, Durham University, South Road, DH1 3LE, UK
- ⁸⁷ Université Paris Cité, CNRS, Astroparticule et Cosmologie, 75013 Paris, France
- ⁸⁸ University of Applied Sciences and Arts of Northwestern Switzerland, School of Engineering, 5210 Windisch, Switzerland
- ⁸⁹ Institut d'Astrophysique de Paris, 98bis Boulevard Arago, 75014, Paris, France
- ⁹⁰ Institut de Física d'Altes Energies (IFAE), The Barcelona Institute of Science and Technology, Campus UAB, 08193 Bellaterra (Barcelona), Spain
- ⁹¹ Department of Physics and Astronomy, University of Aarhus, Ny Munkegade 120, DK-8000 Aarhus C, Denmark
- ⁹² Waterloo Centre for Astrophysics, University of Waterloo, Waterloo, Ontario N2L 3G1, Canada
- ⁹³ Department of Physics and Astronomy, University of Waterloo, Waterloo, Ontario N2L 3G1, Canada
- ⁹⁴ Perimeter Institute for Theoretical Physics, Waterloo, Ontario N2L 2Y5, Canada
- ⁹⁵ Space Science Data Center, Italian Space Agency, via del Politecnico snc, 00133 Roma, Italy
- ⁹⁶ Institute of Space Science, Str. Atomistilor, nr. 409 Măgurele, Ilfov, 077125, Romania
- ⁹⁷ Dipartimento di Fisica e Astronomia "G. Galilei", Università di Padova, Via Marzolo 8, 35131 Padova, Italy
- ⁹⁸ Departamento de Física, FCFM, Universidad de Chile, Blanco Encalada 2008, Santiago, Chile
- ⁹⁹ INFN-Sezione di Roma, Piazzale Aldo Moro, 2 - c/o Dipartimento di Fisica, Edificio G. Marconi, 00185 Roma, Italy
- ¹⁰⁰ Atlantis, University Science Park, Sede Bld 48940, Leioa-Bilbao, Spain
- ¹⁰¹ Institute of Space Sciences (ICE, CSIC), Campus UAB, Carrer de Can Magrans, s/n, 08193 Barcelona, Spain
- ¹⁰² Infrared Processing and Analysis Center, California Institute of Technology, Pasadena, CA 91125, USA
- ¹⁰³ Instituto de Astrofísica e Ciências do Espaço, Faculdade de Ciências, Universidade de Lisboa, Tapada da Ajuda, 1349-018 Lisboa, Portugal
- ¹⁰⁴ Universidad Politécnica de Cartagena, Departamento de Electrónica y Tecnología de Computadoras, Plaza del Hospital 1, 30202 Cartagena, Spain
- ¹⁰⁵ Centre for Information Technology, University of Groningen, P.O. Box 11044, 9700 CA Groningen, The Netherlands
- ¹⁰⁶ Institut de Recherche en Astrophysique et Planétologie (IRAP), Université de Toulouse, CNRS, UPS, CNES, 14 Av. Edouard Belin, 31400 Toulouse, France
- ¹⁰⁷ INFN-Bologna, Via Irnerio 46, 40126 Bologna, Italy
- ¹⁰⁸ IFPU, Institute for Fundamental Physics of the Universe, via Beirut 2, 34151 Trieste, Italy
- ¹⁰⁹ INFN, Sezione di Trieste, Via Valerio 2, 34127 Trieste TS, Italy
- ¹¹⁰ SISSA, International School for Advanced Studies, Via Bonomea 265, 34136 Trieste TS, Italy
- ¹¹¹ Department of Physics and Astronomy, University of British Columbia, Vancouver, BC V6T 1Z1, Canada